Dirac fermion quantum Hall antidot in graphene

Scott M. Mills,[1] Anna Gura,[1] Kenji Watanabe,[2] Takashi Taniguchi,[2] Matthew Dawber,[1] Dmitri V. Averin,[1,*] and Xu Du[1,†]
[1]*Department of Physics and Astronomy, Stony Brook University, Stony Brook New York 11794-3800, USA*
[2]*National Institute for Materials Science, 1-1 Namiki, Tsukuba 305-0044, Japan*

(Received 28 March 2019; revised manuscript received 3 October 2019; published 18 December 2019)

The ability to localize and manipulate individual quasiparticles in mesoscopic structures is critical in experimental studies of quantum mechanics and thermodynamics, and in potential quantum information devices, e.g., for topological schemes of quantum computation. In strong magnetic field, the quantum Hall edge modes can be confined around the circumference of a small antidot, forming discrete energy levels that have a unique ability to localize fractionally charged quasiparticles. Here, we demonstrate a Dirac fermion quantum Hall antidot in a graphene, where charge-transport characteristics can be adjusted through the coupling strength between the contacts and the antidot, from Coulomb blockade dominated tunneling under weak coupling to the effectively noninteracting resonant tunneling under strong coupling. Both regimes are characterized by single-flux and -charge oscillations in conductance persisting up to temperatures over 2 orders of magnitude higher than previous reports in other material systems. Such graphene quantum Hall antidots may serve as a promising platform for building and studying quantum circuits for quantum simulation and computation.

DOI: 10.1103/PhysRevB.100.245130

I. INTRODUCTION

Localization and manipulation of individual quasiparticles play an important role in the studies of quantum mechanics and quantum thermodynamics, and in the applications of quantum information devices. A wide variety of mesoscopic systems, such as quantum dots [1–4], nitrogen-vacancy centers [5,6], superconducting Cooper pair boxes [7–10], superconducting quantum interference devices [11], etc., have been extensively studied for quantum manipulation of charges, spins, and magnetic fluxes. Quantum Hall (QH) antidots, on the other hand, offer a promising approach for localizing quantum Hall quasiparticles. Due to quantum confinement, the chiral one-dimensional (1D) edge mode has its energy quantized into discrete levels, mimicking a large, tunable "artificial atom" which hosts QH quasiparticles. Compared to the other approaches, QH antidots are capable of localizing even exotic quasiparticles with fractional charges and nontrivial exchange statistics. It therefore holds promise for topological schemes of quantum computation [12,13]. Experimentally, pioneering studies of QH antidots have been carried out using GaAs two-dimensional electron gas (2DEG), where localization of integer [14,15] and fractionally charged [16] quasiparticles have been demonstrated. The potential of applying such QH antidots for quantum information applications has also been discussed [17]. On the other hand, due to the small energy-scale associated with Landau level (LL) spacing and energy quantization, the signatures of the localized QH edge states, namely charge and magnetic flux oscillations in conductance across the antidot, are fragile and require very low electron temperature (typically sub-100 mK) [18] to observe. A 2DEG system which can provide more robust localization of QH quasiparticles and stronger coherence is therefore desirable for realizing more complex devices and functionalities.

The development of 2D crystal graphene in the recent decade raised a new opportunity for studying localized QH states in the antidot setup. The Dirac nature of the 2DEG in graphene [19] differs fundamentally from that in GaAs, due to its linear energy dispersion, chirality, and nontrivial Berry's phase. As a result, graphene can achieve high charge-carrier mobilities ($>10^5\,\mathrm{cm}^2/\mathrm{Vs}$) which persist even with densities down to $\sim 10^9\,\mathrm{cm}^{-2}$ without localization. It has a large and energy-independent Fermi velocity ($v_F \approx 10^6 \mathrm{m/s}$), which leads to large LL spacing ($\Delta\varepsilon_{LL} = \sqrt{2e\hbar v_F^2 B} = 35\sqrt{B[\mathrm{T}]}\,\mathrm{meV}$) [20], as well as large quantization energy spacing under confinement. Both are critical factors for realizing robust localization of QH states. Technically, being a single atomic layer, the size of graphene devices may be pushed down to nanometer scale with sharp definition [21]. And, Ohmic electrical contacts with low contact resistance have been routinely achieved both for top contacts [22] and side contacts [23]. Despite all the promising characteristics, earlier works on graphene antidot devices have been largely focused on band-structure engineering [24], semiclassical charge transport in the antidot arrays [25], and on gate-defined quantum dots [26,27]. Charge-transport studies on well-structured graphene-based QH antidots, on the other hand, have not been reported to our knowledge. In this work, we study Dirac electron QH antidots in graphene, and demonstrate robust localization and quantization of QH edge mode in the lowest-LL (LLL), which persist up to 10–100 times higher temperature compared to previous reports.

II. RESULTS AND DISCUSSION

The samples used in this work, illustrated in Fig. 1, are point-contact-coupled antidots embedded in hexagonal boron

*dmitri.averin@stonybrook.edu
†xu.du@stonybrook.edu

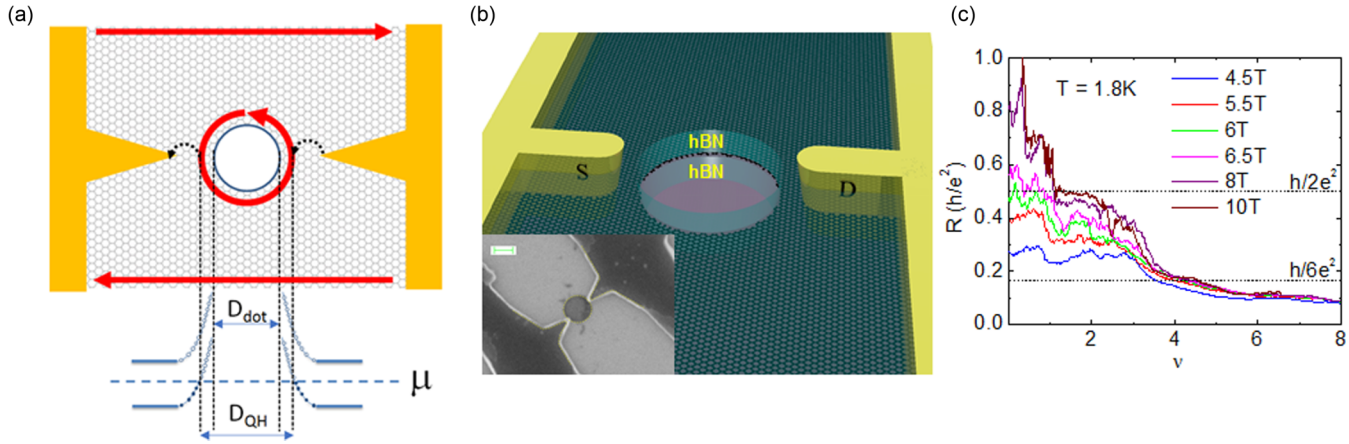

FIG. 1. Graphene QH antidot. (a) Schematics of QH antidot. The red arrows indicate the QH edge states. The band structure illustrates the bulk LLs and the quantized edge states. (b) Structure of a point-contact coupled QH antidot on graphene/hBN heterostructure. Inset: SEM image of a 310-nm-diameter antidot sample. The yellow dotted lines highlight the boundaries of the antidot and the side contacts. The scale bar is 200 nm. The bulk channel edges are outside the view. (c) Two-terminal resistance as a function of filling factor, measured in various fixed magnetic fields by ramping the back-gate voltage.

nitride (hBN)-encapsulated graphene field-effect transistors (see Supplemental Material [28] and references [23] within). The two-terminal conductance consists of a background from the bulk [29,30] and the tunneling conductance through the QH antidot. Under well-developed QH effect, depending on the coupling strength between the point contacts and the antidot, the QH plateau resistances can vary between $\frac{h}{\nu e^2}$ for decoupled antidot, and $\frac{h}{2\nu e^2}$ in the situation when antidot is split by the contacts (see Supplemental Material [28]). In our experiments, the coupling between the point contacts and the antidot is carefully adjusted to be in between these two limits. The overall geometry of our devices is designed so that: (1) the diameter of the antidot $D_{\rm dot} \gg l_B = \sqrt{\frac{\hbar}{eB}}$, where l_B is the magnetic length ∼10 nm for the few-tesla magnetic field applied here; (2) $D_{\rm dot}$ is sufficiently small for energy quantization; (3) the point contacts probing the antidot are sufficiently sharp to minimize invasive effects and to optimize phase-coherent charge transport. Satisfying these criteria, we designed the diameter to be $D_{\rm dot} \sim 200 - 310$ nm and the width of the point contacts to be ∼15 nm. The dimensions of the devices are directly confirmed by scanning electron microscopy (SEM) imaging. Figure 1(c) shows QH resistance as a function of filling factor $\nu = \frac{nh}{eB}$ in various magnetic fields (through ramping of the gate voltage). We note that in measuring these curves the gate-voltage ramping speed is relatively large and the fine oscillatory features (as discussed below) are washed out. At anomalous integer fillings $\nu = 4(n + \frac{1}{2})$, the resistance values are observed to be between $\frac{h}{\nu e^2}$ and $\frac{h}{2\nu e^2}$ due to the conduction through the antidot.

In quantizing magnetic fields, periodic conductance oscillations both in gate voltage and in magnetic field become prevalent at filling factors between $\nu = 1$ and $\nu = 2$, with typical amplitude of $\sim 0.1 G_0$ ($G_0 = \frac{e^2}{h}$ is the conductance quantum). Depending on the coupling distance between the point contacts and the antidot, two types of periodicity are observed which we separately discuss below. In the case of relatively weak coupling, as shown in Fig. 1(b) for a 310-nm-diameter antidot sample with a few tens of nanometers contact-antidot separation, the conductance oscillations under ramping magnetic field show an approximately constant period of 21 mT. In Fig. 2(b), we plot the oscillatory conductance as a function of magnetic flux through the antidot, normalized over single-electron magnetic flux quantum: $\frac{\Phi}{\Phi_0} = \frac{eB\pi D_{\rm QH}^2}{4h}$, where $D_{\rm QH}$ is the diameter of the QH edge current encircling the antidot, and $\Phi_0 = \frac{h}{e}$. With $D_{\rm QH} = 350$ nm, which is slightly larger than the physical diameter of the antidot $D_{\rm dot} = 310$ nm (by the amount consistent roughly with the notion that the edge states are removed from the physical edge by the distance of an order of the magnetic length l_B), the observed conductance oscillations match closely with a flux period of $0.5 \pm 0.1\Phi_0$. We note that the observed $\frac{1}{2}\Phi_0$ flux oscillations are reproducible over repeated thermal cycles and over different samples with similar weak coupling. This suggests their origin to be intrinsic to the antidots, and independent of the unintentional defects.

Corresponding periodic conductance oscillations are also observed as the gate voltage is swept at fixed magnetic field. Figure 2(d) shows the conductance oscillations in the 310-nm antidot as a function of gate voltage and charge-number change over the area of the antidot: $\frac{\Delta Q}{e} = \frac{c\Delta V_G \pi D_{\rm dot}^2}{4e}$. Here c is the geometrical capacitance per area. On average, each conductance oscillation corresponds to addition/removal of one electron into the edge state on the antidot. Compared to the flux oscillations, the charge oscillations appear to be somewhat less regular, indicating the presence of random fluctuations in the coupling capacitance between the back gate and the antidot. Direct correspondence between the charge and flux oscillations is evidenced by Fig. 2(e), where the conductance oscillations form tilted stripes on the "magnetic-field–gate voltage" plane. Along the charge oscillation axis, however, there are significant random fluctuations which manifest the charge noise.

Next, we discuss the antidots with stronger coupling to the point contacts, where a different type of magnetic oscillation periodicity is observed, as illustrated by Fig. 3(a) for a 200-nm-diameter antidot with point contacts touching its

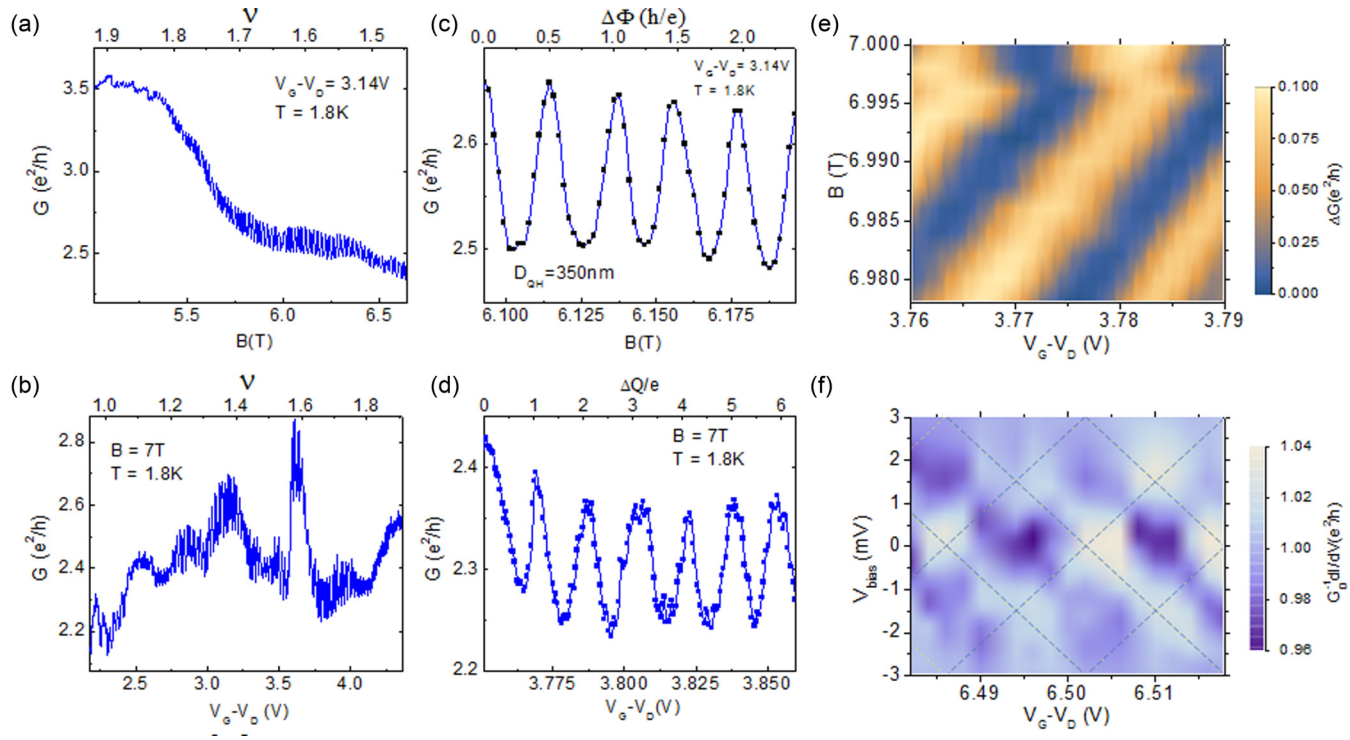

FIG. 2. Coulomb blockade in relatively weakly coupled QH antidot. Conductance oscillations are observed with ramping magnetic field (a) and gate voltage (b). (c) A zoom-in of the conductance oscillations shows a magnetic flux period of $\Phi_0/2$, calculated using a QH edge-state diameter of $D_{\mathrm{QH}} = 350$ nm. (d) A zoom-in of the conductance oscillations shows approximate one oscillation per charge, with charge number calculated using the geometric capacitance over the physical area of the antidot. (e) Conductance oscillations versus both gate voltage and magnetic field. (f) Charge-stability diagram showing Coulomb-blockade characteristics. The dotted lines are guides to the eyes.

circumference (SEM image shown in Supplemental Material [28]). Here, with increasing magnetic field, the conductance oscillations evolve from single-peaks [Fig. 3(a), inset] to "M"-shaped double peaks [Fig. 3(a), main panel]. With an estimated $D_{\mathrm{QH}} \sim$ 225 nm (which again differs from the physical diameter by a size of the order of magnetic length), both the single-peak oscillations in low field and the M-shaped pairs in stronger field match with a flux period of ϕ_0. The flux separation of the two conductance peaks within an M-shaped pair (ΔB_Z) increases with increasing magnetic field, as discussed in detail later. Corresponding to the magnetic oscillations, the gate voltage dependent conductance oscillations in this 200-nm-diameter antidot also show M-shaped pairs, as plotted in Fig. 3(b). The charge period in in this sample is within ~20% of what is calculated using the geometric size of the antidot: $\frac{\Delta Q}{e} = \frac{c\Delta V_G \pi D_{\mathrm{dot}}^2}{4e}$. The discrepancy may be attributed to the errors in the estimations of the antidot size and effective gate capacitance at the antidot.

The observation of Φ_0 period (which obviously also includes the $\frac{1}{2}\Phi_0$ period) of the magnetic flux oscillations strongly suggests Aharonov-Bohm (AB) effect. We note that both charge and flux oscillations are maximized when the Fermi energy is between the zeroth LL and the first LL, and that the oscillations disappear during the plateau-to-plateau transition when the Fermi energy coincides with one of the LLs. This suggests that the oscillations are associated with the QH edge states encircling the antidot. Indeed, clear AB oscillations can be present only if the circulating current has a well-defined diameter. In a QH system, this happens when the Fermi energy is between the LL, and, with the bulk gapped, only the quasi-1D edge modes conduct.

In a single-particle picture (at first, neglecting Zeeman effect), the energy quantization of the finite-size QH edge state is obtained from the single-particle Dirac Hamiltonian $H_0 = v_F \vec{\sigma} \cdot (\vec{p} - e\vec{A}) + U$ with boundary conditions imposed by the antidot geometry (see Supplemental Material [28]). Here $\vec{A} = rB\hat{\varphi}$ is the vector potential in symmetric gauge. The potential energy U is constant in the single-particle picture. Considering the relevant length scales: $D_{\mathrm{dot}} \gg l_B \gg a$ (where $a \sim 0.14$ nm is the lattice constant), the edge state can be approximated as encircling the antidot edge with diameter $D_{\mathrm{QH}} \approx D_{\mathrm{dot}}$. The Dirac Hamiltonian results in magnetic-field-dependent energy levels $\varepsilon_j = \frac{2j\hbar v}{D_{\mathrm{QH}}} + \frac{ev\Phi}{\pi D_{\mathrm{QH}}}$, with constant level spacing (neglecting disorder) $\delta\varepsilon = 2\hbar v/D_{\mathrm{QH}}$. Here $v = -\frac{1}{eB}\frac{dV}{dr} \lesssim v_F$ (V being the confinement potential at the edge) is the velocity of the QH edge state. We note that this relation gives the proper account of the AB effect, as the periodicity of the antidot energy spectrum in magnetic flux has a period equal to the magnetic flux quantum: $\varepsilon_j(\Phi) = \varepsilon_{j-1}(\Phi + \Phi_0)$. And, in graphene, the sharp definition of the antidot facilitates large energy-level spacing $\delta\varepsilon$.

Electron-electron interaction leads to Coulomb-blockade-type effects. In the weak coupling limit ("closed" antidot), the electron interaction energy $U_{ee} = \frac{e^2}{2\pi\epsilon\epsilon_0 L}\ln(\frac{L}{l_B})$, where $L = \pi D_{\mathrm{dot}}$ is the circumference of the edge, is constant for the relevant edge states (see Supplemental Material [28]). For the QH antidots studied in this work, the interaction energy is $U_{ee} = 2.3 - 3.2$ meV, which is much smaller than the

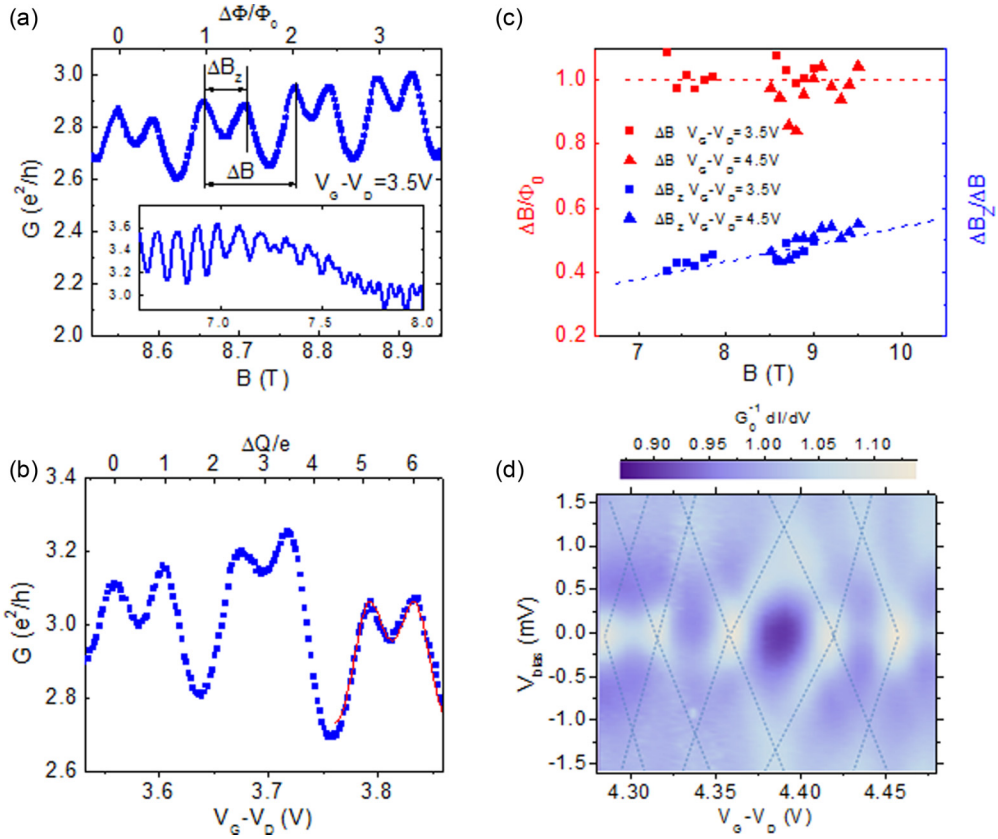

FIG. 3. AB oscillations in strongly coupled QH antidot. (a) Conductance oscillations showing Φ_0 flux period and Zeeman splitting. Inset: In lower magnetic fields, the conductance oscillation evolves from merged peaks with Φ_0 period to M-shaped spin-resolved oscillations, with increasing magnetic field. (b) Conductance oscillations with ramping gate voltage. The top x axis shows the change in charge number calculated using the geometrical capacitance over the physical area of the antidot. The red solid curve shows the fitting to a relatively symmetric M-shaped oscillation using thermal excitation model. (c) Magnetic-field dependences of the AB oscillation period (ΔB) and normalized Zeeman splitting ($\Delta B_Z/\Delta B$). The dotted lines are guides to the eyes. (d) Differential conductance versus bias voltage and gate voltage. Dotted lines are guides to the eyes. From the bias- and gate dependence of the differential conductance, the energy-level spacing is a summation of the bias voltages at the two adjacent diamond tips which correspond to the two spin states.

LL spacing but significantly larger than the Zeeman energy within the range of magnetic fields applied. In the presence of metallic contacts, U_{ee} should be screened and somewhat reduced.

Following the discussion above, the antidot can be described by a many-body Hamiltonian (see Supplemental Material [28] and references [31–36] within):

$$H = \frac{U_{ee}}{2}(n + n_\phi - n_G)^2 + \sum_{j,\sigma} \varepsilon_{j,\sigma} n_{j,\sigma}. \qquad (1)$$

Here $n = \sum_{j,\sigma} n_{j,\sigma}$ is the total charge number associated with the edge states, $n_{j,\sigma}$ is the occupation number of the state with orbital index j, spin index $\sigma = \pm 1$, and the single-particle energy $\varepsilon_{j,\sigma} = \varepsilon_j + g\mu_B B\sigma/2$, where μ_B is the Bohr magneton, B is the magnetic field, and the g factor for electrons in graphene is close to its free-electron value [37] $g \approx 2$. Also in the Hamiltonian, $n_G = cV_G$ and $n_\phi = \frac{\nu_S \Phi}{\Phi_0}$, where ν_S is the number of occupied LLs including spin degeneracy, which gives the number of the propagating edge modes. Periodicity of the linear antidot conductance, or other equilibrium properties of the antidot, in the back-gate voltage V_G or magnetic flux Φ, is determined by the behavior of the occupation factors $n_{j,\sigma}$ and the Hamiltonian H as functions of V_G and Φ under the conditions of the fixed chemical potential of the external contacts to the antidot. Increase of the gate voltage such that $n_G \to n_G + 1$ leads to the corresponding increase of the total occupation factor, $n \to n + 1$, leaving the Hamiltonian invariant, $H(\mathrm{n}_G) = H(\mathrm{n}_G + 1)$. Similarly, because the spin-degenerate single-particle spectrum of the antidot is periodic in flux with the period Φ_0, increase of the flux such that $n_\phi \to n_\phi + \nu_S$ leads to the decrease of the total occupation factor, $n \to n - \nu_S$, leaving the Hamiltonian unchanged, $H(\mathrm{n}_\phi) = H(\mathrm{n}_\phi + \nu_S)$. This gives rise to the observed single-charge periodicity in the gate voltage, and ensures Φ_0 flux periodicity in all regimes in agreement with the general Byers-Yang theorem [38]. With ν_S QH edge modes, and with degeneracy broken in the Coulomb interaction-dominated regime, one expects ν_S conductance peaks per Φ_0. This is evident from Hamiltonian (1) that the single-charge period $\Delta n_\phi = 1$ as a function of magnetic flux gives rise to the finer flux oscillation period $\frac{\Phi_0}{\nu_S}$. Such fractional AB oscillations have been observed in GaAs heterostructures including antidots [14,15] and the related structures, Fabry-Perot interferometers [33,39,40] in the integer quantum Hall regime.

For a relatively weakly coupled (closed) antidot ([e.g., the 310-nm-diameter antidot sample in Fig. 1(b)] and with the Fermi energy above the LLL ($\nu_S = 2$), equally spaced magnetic oscillations are observed with $\Phi_0/2$ period (consistent with the larger period Φ_0) independent of magnetic field. This suggests that the antidot tunneling is dominated by electron-electron interaction which results in a constant energy gap for the addition of individual electrons to the antidot that is independent, e.g., of electron spin. To find this addition energy, we measured the bias-voltage dependence of the device conductance. In Fig. 2(f), we plot the background-normalized differential conductance (dI/dV) as a function of gate voltage and bias voltage (charge-stability diagram), which resembles the Coulomb blockade diamonds, revealing the charge addition energy to be ∼1.5 meV for the 310-nm-diameter antidot sample. We note that the quality of the charge-stability diagram is limited by the charge noise in the sample and the electrical noise in our measurement setup. Well-defined periodicity of the conductance oscillations in this antidot implies that the addition energy is given by the Coulomb repulsion energy U_{ee}, with the single-particle energy-level spacing $\sim\delta\varepsilon$ either too small to be noticeable in comparison to U_{ee}, or washed out by electron-electron relaxation. Compared to a simple closed-antidot estimate of ∼2.3 meV, the observed Coulomb repulsion energy is somewhat smaller, which can be qualitatively explained by finite screening effect from the contacts.

For a strongly coupled ("open") antidot, the electron-electron interaction is largely screened by the electrodes. Neglecting electron correlations, the single-particle picture of energy-level quantization and Zeeman splitting predicts AB oscillation with a primary oscillation period of Φ_0 and a B-dependent Zeeman splitting of the conductance peaks in strong magnetic fields [41]. This is indeed consistent with our observation where single-flux oscillations in weak magnetic field split and resolve into M-shaped pairs in strong magnetic field. In Fig. 3(c), the conductance oscillation period in magnetic field is plotted as a function of magnetic field, both for the M-shaped pairs (ΔB) and for the magnetic-field splitting within each pair (ΔB_Z). ΔB is roughly magnetic-field independent with its corresponding flux period $\sim\Phi_0$. The magnetic-field dependence of ΔB_Z can be fit to a straight line intersecting the origin. Extrapolating the linear dependence, $\Delta B_Z\ (B_0)\frac{\pi D_{\rm QH}^2}{4} = \Phi_0$, we get $B_0 \sim 18.5$ T at which Zeeman splitting becomes equal to the quantization energy spacing $\delta\varepsilon = 2\hbar v/D_{\rm QH}$. Based on this comparison, we can estimate $\delta\varepsilon = g\mu_B B_0 \sim 2.1$ meV. This value is confirmed by measuring the bias and gate dependence of the differential conductance [Fig. 3(d)] where the level-spacing energy is a sum of the heights of the two adjacent "diamonds" (from Zeeman splitting) in the plot, which gives ∼2–2.5 meV. From the level spacing, we can estimate the QH edge-state velocity $v \sim 3.4 \times 10^5$ m/s , about 1/3 of the Fermi velocity of free Dirac electrons in graphene.

In the Coulomb blockade dominated regime, the conductance oscillations are suppressed at elevated temperatures through thermal excitation/smearing [Fig. 4(a)]. The corresponding antidot conductance can be calculated numerically through the linear response of the Coulomb blockade rate equations [32] to the external bias (see Supplemental Material [28]). Figure 4(b) shows the temperature dependence of the averaged conductance oscillation amplitude (defined as the difference in conductance at successive minima and maxima), with the best fit calculated numerically with addition energy U_{ee} and a normalization prefactor as fitting parameters. The best fit of the addition energy, $U_{ee} = 1.3$ meV, is in good agreement with the value obtained experimentally from the height of the Coulomb diamonds for the 310-nm antidot sample [Fig. 2(f)]. As is characteristic of single-electron devices, the linear conductance oscillations are nearly completely suppressed as the temperature exceeds half of the addition energy.

We note that in the weakly coupled QH antidot discussed above, the Coulomb oscillations persist up to ∼4 K, which is 1–2 orders of magnitude higher than the previous reports for GaAs-based devices with comparable antidot size. The robustness of single charging effects can be further enhanced by increasing the electron-electron interaction energy U_{ee}. To demonstrate this, we study a QH antidot sample with ∼250-nm effective diameter made on suspended graphene, where U_{ee} is enhanced through a reduction in dielectric screening. In the suspended graphene sample, carrier mobility can be sequentially improved through repeated current annealing (controlled Joule heating which evaporates the contaminants). Rather than coupling to the antidot using protruding point contacts (which induces unwanted high current density at the sharp tips, causing damage during the annealing), straight source and drain electrodes are used which are separated from the antidot by ∼200 nm [Fig. 4(d), inset]. Coupling to the antidot is possible only in low magnetic fields, through extended states from the electrodes. With high mobility $>10^5$ cm^2/Vs, QH plateaus become well developed in magnetic field as low as 1 T. Figure 4(d) shows the conductance oscillations in gate voltage at $B = 1$ T. The antidot is weakly coupled as is evident from the nearly unperturbed QH plateau resistance background [Fig. 4(d)]. A thorough current annealing narrows the conductance peaks, as shown by Fig. 4(e). In absence of the hBN encapsulation, the effective dielectric constant and screening becomes significantly reduced, resulting in a much larger Coulomb gap. In Fig. 4(f), the charge-stability diagram measures a Coulomb gap of ∼8 meV. The large Coulomb gap allows single-charge oscillations to persist for temperatures over 10 K, as shown in Fig. 4(e). In Fig. 4(f), we also observe evidence of energy quantization in the excited states, indicated by the bright lines outside the Coulomb diamonds. The energy level spacing $\delta\varepsilon$ is found to be ∼5 meV, and is spin degenerate due to the small magnetic field. Formation of such quantized energy levels suggests robust coherence in these high-mobility samples.

For samples with strong coupling to the antidot, where Coulomb blockade is largely screened, both thermal excitation and disorder can contribute to the suppression of conductance oscillations (see Supplemental Material [28]). Inelastic charge-carrier scattering, including electron-electron and electron-phonon scattering, have a characteristic energy scale of $\sim k_B T$ which is much smaller than the energy-level spacing $\delta\epsilon \approx 2$ meV for the 200-nm antidot. Consequently, decoherence is not expected to play a critical role in the temperature dependence of conductance oscillations. In the strong tunneling limit, the amplitude of the conductance oscillations can be calculated using a standard double-barrier transmission

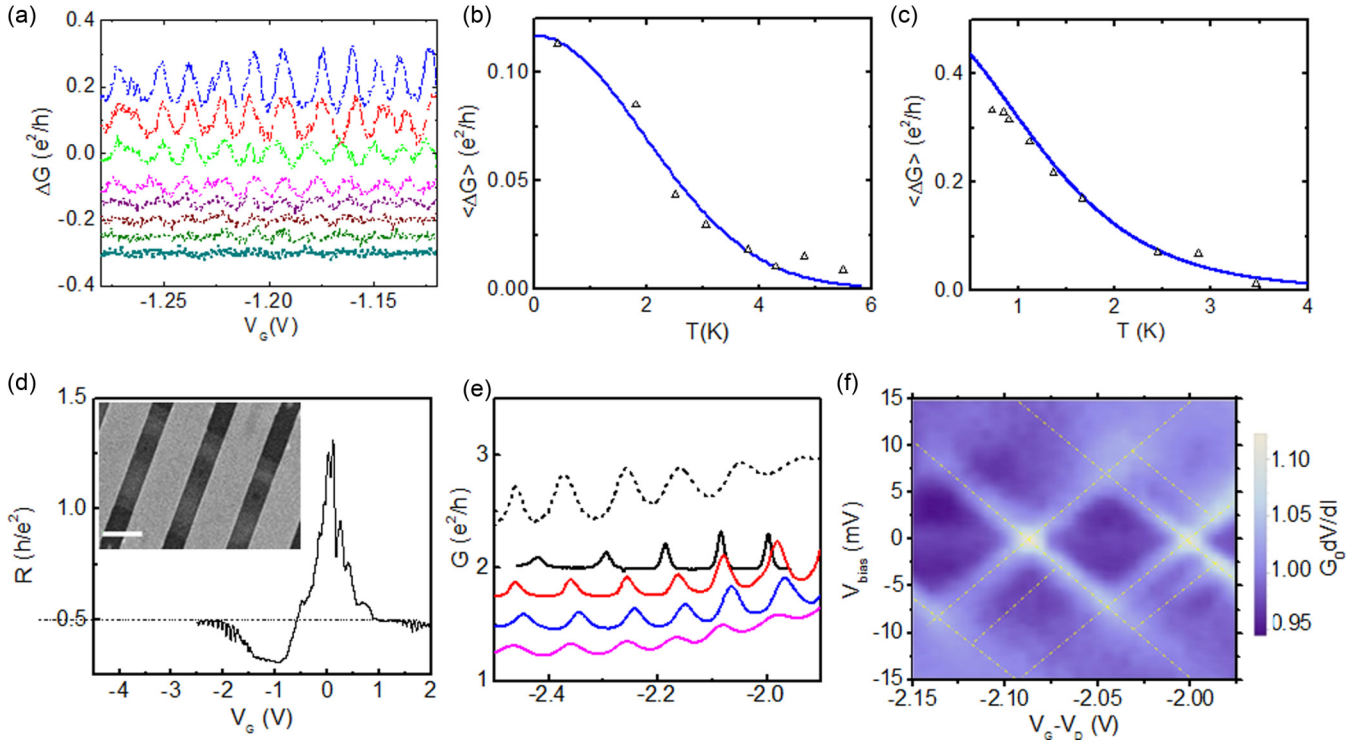

FIG. 4. Thermal suppression of conductance oscillations in the QH antidots. (a) Gate-dependent conductance oscillation at various temperatures. The curves, taken at (from top to bottom) $T = 0.4$, 1.8, 2.5, 3.1, 3.8, 4.3, 4.8, and 5.5 K, are vertically shifted for clarity. The temperature dependence of the averaged conductance oscillation amplitude for the weakly coupled 310-nm antidot (b) and the strongly coupled 200-nm antidot (c) are fitted with thermal excitation models. (d) Conductance oscillations in a suspended graphene QH antidot at $B = 1$ T. The dotted line labels QH plateau resistance at $n = 2$. Inset: SEM image of a suspended graphene with three QH antidot devices. The scale bar is 1 μm. (e) Temperature dependence of conductance oscillations. The dotted and the solid black curves, both measured at 450 mK, correspond to before and after thorough current annealing, respectively. The red, blue, and purples curves are taken at 2, 5, and 10 K, respectively, and are shifted downward for clarity. (f) Charge-stability plot for the suspended graphene QH antidot, taken in 1-T magnetic field at 450 mK. The dotted lines are guides to the eyes.

model, characterized by the transmission probabilities at the two leads. In the LLL at fixed magnetic field, the two modes for each spin contribute in parallel with a relative shift given by the Zeeman energy. Increasing temperature in the two leads then effectively smears the energy levels and causes suppression of the amplitude of conductance oscillations (see Supplemental Material [28]). In Fig. 3(b) we fit the gate dependence of an M-shaped oscillation pair at $B = 8.5$ T, using 0.85 and 0.51 as the transmission probabilities, and a Zeeman splitting of 0.82 meV which is in reasonable agreement with $g\mu_B B = 0.98$ meV. In Fig. 4(c), the temperature dependence of the averaged conductance oscillation amplitude at $B = 10$ T is calculated using the thermal excitation model and compared with the experimental data, with transmission probabilities 0.72 and 0.41. The deviation of the simulation from the conductance oscillation amplitude data at low temperatures ($T < 1$ K) may be an indication of the charge noise in the vicinity of the antidot, which provides an additional mechanism of suppression of the conductance oscillations that becomes noticeable once the thermal broadening is weak.

In all our discussions above, we have not considered the interchannel scattering which can happen on the etching-defined physical edges of the antidots. It has been shown that such interchannel scattering can happen between the same-spin edge modes and causes equilibration of the modes [37]. In our measurements which focus on the lowest Landau level, the two edge channels have opposite spins, hence edge-channel equilibration is not expected.

III. CONCLUSION

We demonstrate an experimental study on Dirac electron quantum Hall antidots in graphene. Depending on the coupling strength to the antidot, both Coulomb blockade dominated tunneling and effectively noninteracting resonant tunneling are achieved. Both regimes are characterized by single-flux and single-charge oscillations in conductance which, due to the Dirac nature of the electron gas in graphene and its capability of defining the antidot structure with great sharpness, persist up to temperatures over 2 orders of magnitude higher than that reported previously on conventional 2D electron gas.

The main advantages of using graphene in QH antidots come from its large edge-state velocity v (as a result of the Dirac spectrum), which results in the large energy-level spacing, and large Landau-level separation which permits scaling up of the characteristic antidot energies. Another technical convenience of graphene in QH antidot samples comes from the observation that the diameter of the QH edge state encircling the antidot is very close to the physical

size. All this opens the possibility of precise design of the antidots and their coupling into multiple antidot structures for possible applications in quantum information. We note that while in this work we mainly focused on direct metallic point contacts, coupling to the antidot can also be achieved through the more conventional QH edge-to-edge tunneling (see Supplemental Material [28]). With further work to optimize the device structure and mobility, the graphene QH antidot system demonstrated here may serve as a promising platform for studying localized QH states, and for building antidot-based quantum circuits for quantum simulation and computation. Besides graphene, the chiral edge-state-based antidot structure can also be applied in many other 2D systems (e.g., 2D superlattice, layered topological material, etc.), providing an effective technique for studying chiral quasiparticles.

ACKNOWLEDGMENTS

This work was supported by US National Science Foundation under Award DMR-1836707. K.W. and T.T. acknowledge support from the Elemental Strategy Initiative conducted by the MEXT, Japan and the CREST (Grant No. JPMJCR15F3). J.S.T., S.M., and X.D. acknowledge Vladimir Goldman for insightful discussions.

[1] A. P. Alivisatos, Semiconductor clusters, nanocrystals, and quantum dots, Science **271**, 933 (1996).

[2] Y. Narukawa, Y. Kawakami, M. Funato, S. Fujita, S. Fujita, and S. Nakamura, Role of self-formed InGaN quantum dots for exciton localization in the purple laser diode emitting at 420 nm, Appl. Phys. Lett. **70**, 981 (1997).

[3] M. Veldhorst, J. C. C. Hwang, C. H. Yang, A. W. Leenstra, B. de Ronde, J. P. Dehollain, J. T. Muhonen, F. E. Hudson, K. M. Itoh, A. Morello, and A. S. Dzurak, An addressable quantum dot qubit with fault-tolerant control-fidelity, Nat. Nanotechnol. **9**, 981 (2014).

[4] J. Yoneda, K. Takeda, T. Otsuka, T. Nakajima, M. R. Delbecq, G. Allison, T. Honda, T. Kodera, S. Oda, Y. Hoshi, N. Usami, K. M. Itoh, and S. Tarucha, A quantum-dot spin qubit with coherence limited by charge noise and fidelity higher than 99.9%, Nat. Nanotechnol. **13**, 102 (2018).

[5] M. V. Gurudev Dutt, L. Childress, L. Jiang, E. Togan, J. Maze, F. Jelezko, A. S. Zibrov, P. R. Hemmer, and M. D. Lukin, Quantum register based on individual electronic and nuclear spin qubits in diamond, Science **316**, 1312 (2007).

[6] L. Childress, M. V. Gurudev Dutt, J. M. Taylor, A. S. Zibrov, F. Jelezko, J. Wrachtrup, P. R. Hemmer, and M. D. Lukin, Coherent dynamics of coupled electron and nuclear spin qubits in diamond, Science **314**, 281 (2006).

[7] D. V. Averin, A. B. Zorin, and K. K. Likharev, Bloch oscillations in small Josephson junctions, Zh. Eksp. Teor. Fiz. **88**, 692 (1985) [Sov. Phys. JETP **61**, 407 (1985)].

[8] M. Büttiker, Zero-current persistent potential drop across small-capacitance Josephson junctions, Phys. Rev. B **36**, 3548 (1987).

[9] V. Bouchiat, D. Vion, P. Joyez, D. Esteve, and M. H. Devoret, Quantum coherence with a single Cooper pair, Phys. Scr. **T76**, 165 (1998).

[10] Y. Nakamura, Yu. A. Pashkin, and J. S. Tsai, Coherent control of macroscopic quantum states in a single-Cooper-pair box, Nature (London) **398**, 786 (1999).

[11] J. R. Friedman, V. Patel, W. Chen, S. K. Tolpygo, and J. E. Lukens, Quantum superposition of distinct macroscopic states, Nature (London) **406**, 43 (2000).

[12] C. Nayak, S. H. Simon, A. Stern, M. Freedman, and S. D. Sarma, Non-Abelian anyons and topological quantum computation, Rev. Mod. Phys. **80**, 1083 (2008).

[13] S. D. Sarma, M. Freedman, and C. Nayak, Topologically Protected Qubits from a Possible Non-Abelian Fractional Quantum Hall State, Phys. Rev. Lett. **94**, 166802 (2005).

[14] V. J. Goldman, J. Liu, and A. Zaslavsky, Electron tunneling spectroscopy of a quantum antidot in the integer quantum Hall regime, Phys. Rev. B **77**, 115328 (2008).

[15] M. Kataoka, C. J. B. Ford, G. Faini, D. Mailly, M. Y. Simmons, D. R. Mace, C. T. Liang, and D. A. Ritchie, Detection of Coulomb Charging Around an Antidot in the Quantum Hall Regime, Phys. Rev. Lett. **83**, 160 (1999).

[16] V. J. Goldman and B. Su, Resonant tunneling in the quantum Hall regime: Measurement of fractional charge, Science **267**, 1010 (1995).

[17] D. V. Averin and V. J. Goldman, Quantum computation with quasiparticles of the fractional quantum Hall effect, Solid State Commun. **121**, 25 (2001).

[18] I. Karakurt, V. J. Goldman, J. Liu, and A. Zaslavsky, Absence of Compressible Edge Channel Rings in Quantum Antidots, Phys. Rev. Lett. **87**, 146801 (2001).

[19] A. H. Castro Neto, F. Guinea, N. M. R. Peres, K. S. Novoselov, and A. K. Geim, The electronic properties of graphene, Rev. Mod. Phys. **81**, 109 (2009).

[20] K. S. Novoselov, Z. Jiang, Y. Zhang, S. V. Morozov, H. L. Stormer, U. Zeitler, J. C. Maan, G. S. Boebinger, P. Kim, and A. K. Geim, Room-temperature quantum hall effect in graphene, Science **315**, 1379 (2007).

[21] B. S. Jessen, L. Gammelgaard, M. R. Thomsen, D. M. A. Mackenzie, J. D. Thomsen, J. M. Caridad, E. Duegaard, K. Watanabe, T. Taniguchi, T. J. Booth, T. G. Pedersen, A.-P. Jauho, and P. Bøggild, Lithographic band structure engineering of graphene, Nat. Nanotechnol. **14**, 340 (2019).

[22] A. Allain, J. Kang, K. Banerjee, and A. Kis, Electrical contacts to two-dimensional semiconductors, Nat. Mater. **14**, 1195 (2015).

[23] L. Wang, I. Meric, P. Y. Huang, Q. Gao, Y. Gao, H. Tran, T. Taniguchi, K. Watanabe, L. M. Campos, D. A. Muller, J. Guo, P. Kim, J. Hone, K. L. Shepard, and C. R. Dean, One-dimensional electrical contact to a two-dimensional material, Science **342**, 614 (2013).

[24] J. A. Fürst, J. G. Pedersen, C. Flindt, N. A. Mortensen, M. Brandbyge, T. G. Pedersen, and A. P. Jauho, Electronic properties of graphene antidot lattices, New J. Phys. **11**, 095020 (2009).

[25] A. Sandner, T. Preis, C. Schell, P. Giudici, K. Watanabe, T. Taniguchi, D. Weiss, and J. Eroms, Ballistic transport in graphene antidot lattices, Nano Lett. **15**, 8402 (2015).

[26] C. Gutiérrez, D. Walkup, F. Ghahari, C. Lewandowski, J. F. Rodriguez-Nieva, K. Watanabe, T. Taniguchi, L. S. Levitov,

N. B. Zhitenev, and J. A. Stroscio, Interaction-driven quantum Hall wedding cake–like structures in graphene quantum dots, Science **361**, 789 (2018).

[27] N. M. Freitag, L. A. Chizhova, P. Nemes-Incze, C. R. Woods, R. V. Gorbachev, Y. Cao, A. K. Geim, K. S. Novoselov, J. Burgdörfer, F. Libisch, and M. Morgenstern, Electrostatically confined monolayer graphene quantum dots with orbital and valley splittings, Nano Lett. **16**, 5798 (2016).

[28] See Supplemental Material at http://link.aps.org/supplemental/10.1103/PhysRevB.100.245130 for device fabrication, characterizations, and modeling.

[29] M. Ben Shalom, M. J. Zhu, V. I. Fal'ko, A. Mishchenko, A. V. Kretinin, K. S. Novoselov, C. R. Woods, K. Watanabe, T. Taniguchi, A. K. Geim, and J. R. Prance, Quantum oscillations of the critical current and high-field superconducting proximity in ballistic graphene, Nat. Phys. **12**, 318 (2015).

[30] J. R. Williams, D. A. Abanin, L. DiCarlo, L. S. Levitov, and C. M. Marcus, Quantum Hall conductance of two-terminal graphene devices, Phys. Rev. B **80**, 045408 (2009).

[31] A. R. Akhmerov and C. W. J. Beenakker, Boundary conditions for Dirac fermions on a terminated honeycomb lattice, Phys. Rev. B **77**, 085423 (2008).

[32] D. V. Averin and K. K. Likharev, in *Modern Problems in Condensed Matter Sciences*, edited by B. L. Altshuler, P. A. Lee, and R. A. Webb (Elsevier, Amsterdam, 1991), Chap. 6, pp. 173–271.

[33] P. Delplace and G. Montambaux, WKB analysis of edge states in graphene in a strong magnetic field, Phys. Rev. B **82**, 205412 (2010).

[34] D. P. DiVincenzo and E. J. Mele, Self-consistent effective-mass theory for intralayer screening in graphite intercalation compounds, Phys. Rev. B **29**, 1685 (1984).

[35] M. O. Goerbig, Electronic properties of graphene in a strong magnetic field, Rev. Mod. Phys. **83**, 1193 (2011).

[36] M. Stone, Schur functions, chiral bosons, and the quantum-Hall-effect edge states, Phys. Rev. B **42**, 8399 (1990).

[37] M. B. Lundeberg and J. A. Folk, Spin-resolved quantum interference in graphene, Nat. Phys. **5**, 894 (2009).

[38] N. Byers and C. N. Yang, Theoretical Considerations Concerning Quantized Magnetic Flux in Superconducting Cylinders, Phys. Rev. Lett. **7**, 46 (1961).

[39] Y. Zhang, D. T. McClure, E. M. Levenson-Falk, C. M. Marcus, L. N. Pfeiffer, and K. W. West, Distinct signatures for Coulomb blockade and Aharonov-Bohm interference in electronic Fabry-Perot interferometers, Phys. Rev. B **79**, 241304(R) (2009).

[40] C. J. B. Ford, P. J. Simpson, I. Zailer, D. R. Mace, M. Yosefin, M. Pepper, D. A. Ritchie, J. E. F. Frost, M. P. Grimshaw, and G. A. C. Jones, Charging and double-frequency Aharonov-Bohm effects in an open system, Phys. Rev. B **49**, 17456 (1994).

[41] M. Kato, A. Endo, S. Katsumoto, and Y. Iye, Spin-resolved edge states around an antidot in the vicinity of the $\nu = 2$ quantum Hall state, J. Phys. Soc. Jpn. **78**, 124704 (2009).